SENSITIVITY OF HOSTILE HEMODYNAMICS TO ANEURYSM GEOMETRY VIA UNSUPERVISED SHAPE INTERPOLATION*

Daniel E. MacDonald[1], Nicole M. Cancelliere[2], Vitor M. Pereira[2], and David A. Steinman[1]

[1]Department of Mechanical & Industrial Engineering, University of Toronto
5 King's College Rd, Toronto, Ontario, Canada, M5S 3G8
[2]Department of Neurosurgery, St. Michael's Hospital
36 Queen St E, Toronto, Ontario, Canada, M5B 1W8

ABSTRACT

Background and Objective Vessel geometry and hemodynamics are intrinsically linked, whereby geometry determines hemodynamics, and hemodynamics influence vascular remodelling. Both have been used for testing clinical outcomes, but geometry/morphology generally has less uncertainty than hemodynamics derived from medical image-based computational fluid dynamics (CFD). To provide clinical utility, CFD-based hemodynamic parameters must be robust to modelling errors and/or uncertainties, but must also provide useful information not more-easily extracted from shape alone. The objective of this study was to methodically assess the response of hemodynamic parameters to gradual changes in shape created using an unsupervised 3D shape interpolation method.

Methods We trained the neural network NeuroMorph on 3 patient-derived intracranial aneurysm surfaces (labelled A, B, C), and then generated 3 distinct morph sequences ($A \rightarrow B$, $B \rightarrow C$, $C \rightarrow A$) each containing 10 interpolated surfaces. From high-fidelity CFD simulation of these, we calculated a variety of common reduced hemodynamic parameters, including many previously associated with aneurysm rupture, and analyzed their responses to changes in shape, and their correlations.

Results The interpolated surfaces demonstrate complex, gradual changes in branch angles, vessel diameters, and aneurysm morphology. CFD simulation showed gradual changes in aneurysm jetting characteristics and wall-shear stress (WSS) patterns, but demonstrated a range of responses from the reduced hemodynamic parameters. Spatially and temporally averaged parameters including time-averaged WSS, time-averaged velocity, and low-shear area (LSA) showed low variation across all morph sequences, while parameters of flow complexity such as oscillatory shear, spectral broadening, and spectral bandedness indices showed high variation between slightly-altered neighboring surfaces. Correlation analysis revealed a great deal of mutual information with easier-to-measure shape-based parameters.

Conclusions In the absence of large clinical datasets, unsupervised shape interpolation provides an ideal laboratory for exploring the delicate balance between robustness and sensitivity of nominal hemodynamic predictors of aneurysm rupture. Parameters like time-averaged WSS and LSA that are highly "robust" may, as a result, be effectively redundant to morphological predictors, whereas more sensitive parameters may be too uncertain for practical clinical use. Understanding these sensitivities may help identify parameters that are capable of providing added value to rupture risk assessment.

Keywords machine learning · intracranial aneurysm · computational fluid dynamics · geometry · morphology · uncertainty quantification

*Citation: This article has been accepted for publication in *Computer Methods and Programs in Biomedicine* (2023) following peer review, and the Version of Record can be accessed online at https://doi.org/10.1016/j.cmpb.2023.107762.

1 Introduction

The growth and development of intracranial aneurysms (hereafter simply aneurysms) is widely believed to be driven by flow-induced progressive degradation of the wall [1]. Such complex cerebrovascular flows cannot easily be resolved using medical imaging alone, but are now routinely simulated using medical-image-based computational fluid dynamics (CFD) [2]. Hemodynamic parameters derived from these simulations are used for rupture association and prediction studies [3, 4, 5]; however, such "patient-specific" CFD is known to be subject to numerous assumptions and uncertainties [6, 7]. Of particular note, they often lack patient-specific flow rates or constitutive properties, leaving geometry as the only patient-derived component of these simulations.

Recent studies suggest that morphology may be a better predictor of aneurysm rupture than many common hemodynamic parameters, and that prediction models using both morphological and hemodynamic parameters perform only slightly better than using morphology alone [8, 4, 3]. This suggests three (non-disjunct) possibilities: (1: *mutual information*) morphological parameters and hemodynamic parameters share a great deal of *mutual information*; (2: *noisy*) hemodynamic parameters may be *noisy* and uncertain due to modelling assumptions, and/or; (3: *divergent*) small changes in geometry can sometimes truly lead to unanticipated, *divergent* changes in hemodynamic parameters. Each of these three possibilities may affect quantified hemodynamic parameters to varying degrees. If a given hemodynamic parameter has a mechanistic connection to rupture and (1: *mutual information*) is true, then the parameter may not provide substantial predictive benefit over geometry alone; if (2: *noisy*) is true, then reducing modelling uncertainty should improve rupture prediction; if (3: *divergent*) is true, then prohibitively large datasets may be required to establish associations or predict rupture. Finding methods for evaluating this morphological-hemodynamic discrepancy would impact the search for clinically relevant hemodynamic predictors of aneurysm rupture.

Previous research has used synthetic and/or modified cerebrovascular geometries to study hemodynamic responses to changes in geometry. Lauric et al. [9, 10] parametrically narrowed the parent artery segment of a synthetic aneurysm model and evaluated the response in hemodynamics. Bruning et al. [11] studied the uncertainty associated with pressure drops across an aortic coarctation by manually narrowing or widening the coarctation by one image voxel in the segmented image. Kjeldsberg et al. [12] created a tool (MorphMan) for high-level modification of any tubular structure based on the underlying Voronoi diagram. Capellini et al. [13] used a radial basis function approach to "morph" between a healthy aorta model and an aneurysmatic aorta model, creating intermediate surfaces with varying levels of aneurysm "bulge", to study differences in hemodynamics in response to synthetic aneurysm growth.

In any of these parameterized approaches, it is reasonable to assume that similar morphologies should produce similar hemodynamics, i.e., there is some degree of *continuity* and predictability between geometry and hemodynamics. By varying a geometric parameter (e.g. aortic "bulge") and quantifying the hemodynamic response at each intermediate surface, these approaches assess the characteristics of this *continuity* (at least with respect to the geometric parameter). As the parameter is modified, we might expect the hemodynamic response to show "low variation" (i.e., no change or only monotonic changes between intermediate surfaces), "medium variation" (i.e., smooth response, but demonstrating local extrema), or "high variation" (i.e., having a high degree of variability between neighboring surfaces). Hemodynamic parameters characterized by medium-to-high variation could either be more uncertain, or could contain relevant diagnostic information that is not present in the geometry alone; low variation parameters may have less uncertainty, but also may contain less information. If we were to vary *many* geometric parameters at once, we might expect complex interactions to occur that could truly lead to unanticipated, *divergent* changes in hemodynamic parameters.

Recent works in machine learning and computer graphics show excellent results for non-rigid deformation and registration (i.e., "morphing") of 3D surfaces [14, 15]. This motivated us to leverage these methods as a new way to augment biomedical datasets for fluid simulation to better investigate the relationship between geometry and fluid flow. In particular, Eisenburger et al. [14] previously introduced the deep neural network NeuroMorph as an unsupervised method for interpolation of triangulated 3D surfaces. After training NeuroMorph on a dataset of (any number of) triangulated surfaces, the network takes as input a source mesh X and target mesh Y and generates a probabilistic correspondence matrix (Π) mapping each vertex in X to a vertex in Y, and an "interpolation flow" ($\Delta(\tau)$) that shifts the source vertices smoothly to the target vertices:

$$X(\tau) \coloneqq X + \Delta(\tau) \tag{1}$$

where $\tau \in [0, 1]$, $X(\tau)$ is an interpolated surface, $X(0) = X$ and $X(1) \approx \Pi Y$. Given a correspondence matrix Π alone, one could linearly interpolate the vertices between X and Y, but this would not necessarily produce geometrically plausible deformations. Using NeuroMorph, Π and $\Delta(\tau)$ are jointly learned using loss functions that penalize unphysical deformations such as large local distortions or surface intersections. Eisenburger et al. showed that the network can create plausible unsupervised interpolations between various 3D surfaces that contain only ab-

stract correspondences, eg, interpolating between a cow and pig [14]. For further details including NeuroMorph's network architecture, mathematical descriptions of the loss functions, and training and implementation details, the reader is referred to [14]. In this paper, we demonstrate an application of NeuroMorph to create plausible interpolations between cerebrovascular aneurysm datasets. By morphing between patient-derived cerebrovascular geometries, we are essentially encapsulating a wide variety of geometric parameters into a single parameter (τ), which allows us to evaluate the hemodynamic response to smooth, non-specific changes in geometry. This *computer experiment* using a dense parameterized dataset allows us to test our assumptions about the *continuity* and sensitivity of hemodynamic parameters to changes in geometry in a way that is not feasible in a sparse real-world dataset. Assessing this *continuity* has implications for understanding the discrepancies in aneurysm rupture prediction specifically, and understanding the complex interactions between morphological parameters more generally.

2 Materials and Methods

2.1 Data selection and preparation

We selected three anterior cerebral artery (ACA) bifurcation aneurysms (labelled A, B, and C) derived from a previous clinical dataset of 60 cases [16] chosen based on their apparent morphological similarity but having demonstrably different flow patterns [17], and because the ACA was the most prevalent site of aneurysms in that consecutive cohort. We recreated NeuroMorph's MATLAB-based data preprocessing routines [18] in Python, relying on PyVista [19], numpy [20], scipy [21], PyGeodesic [22], ACVD [23], MeshFix [24], and VMTK [25]. NeuroMorph requires each surface to contain the same number of vertices. In the original authors' preprocessing implementation, they remesh each surface uniformly; for our aneurysm surfaces, this would mean that aneurysms of different size would have a different number of vertices. To reduce the potential for mesh intersection artifacts in our aneurysm surfaces, we remeshed each surface non-uniformly with an approximately similar number of vertices for the aneurysm sac and for each branch. Using a total of 3000 vertices, we allocated $\sim$500 to each of the five branch segments and $\sim$500 to the aneurysm sac.

2.2 Training NeuroMorph

After preprocessing the surfaces, we trained NeuroMorph on all three surfaces for 75 000 iterations using the default selection of hyperparameters on an Nvidia Titan RTX GPU with 24 GB of memory. Once trained, the network can generate a correspondence matrix and interpolation flow between any pair of those surfaces. As observed in the loss curve of Fig Fig. 1, we intentionally "overfit" the network until losses stopped reducing in an effort to maximize the quality of the correspondence matrices Π.

2.3 Preparing surfaces for CFD

After learning the correspondence matrix Π and interpolation flow $\Delta(\tau)$, we use the network to produce interpolations $X(\tau)$ as in Eq. (1). Note, however, that the interpolated surface $X(1)$ is only an *approximation* of Y; in the present paper, we will use the notation $X \rightarrow Y'$ to indicate the realized sequence of triangulated surfaces from X to the approximated target Y'.

The sequences $A \rightarrow B'$, $B \rightarrow C'$, and $C \rightarrow A'$ can be observed in Fig. 2. The interpolated surfaces tend to preserve the high-frequency shape characteristics of the source surface (such as sac blebs), while adapting the low-frequency characteristics of the target surface (such as branch angles). To prepare each of these sequences for CFD, we set branch clipping points for the original meshes A, B, and C, and linearly interpolated between these points to clip the interpolations. Meshing and simulation were otherwise carried out identically to the strategy previously described in [17] using an average of 2.3 million first-order (P1-P1) tetrahedral elements in each simulation, a level previously verified to provide high-fidelity CFD results [26].

2.4 Statistical analysis

For each of the three sequences in Fig. 2, we quantify various morphological and hemodynamic parameters, and plot them as a function of τ. To explore potential associations between parameters, we calculated the matrix of Pearson correlation coefficients for each sequence. To provide an estimate of the consensus of these correlations across the three sequences, we calculate the average correlation matrix and visualize it using hierarchical clustering (using the `linkage` and `fcluster` methods of `scipy.cluster`) to identify clusters of consistently correlated parameters.

As summarized in Table 1, for each of the three sequences we quantified various morphological and scalar hemodynamic parameters as a function of τ. To explore potential associations between parameters, we calculated the matrix

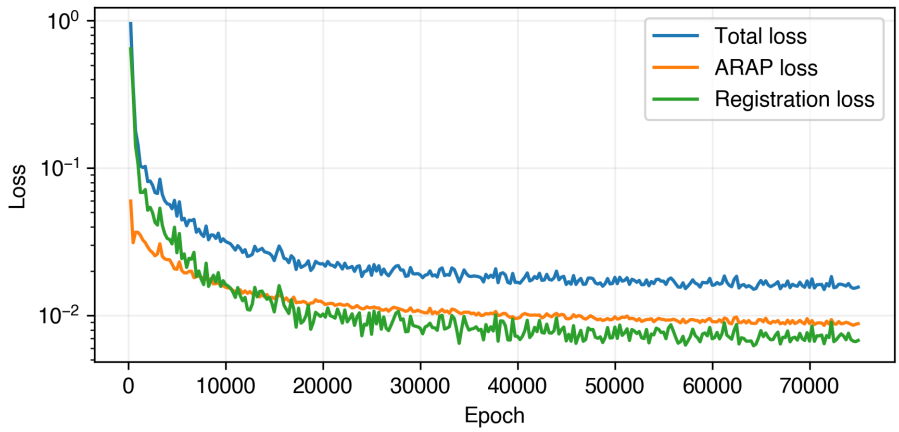

Figure 1: Training loss of NeuroMorph. The as-rigid-as-possible (ARAP) loss penalizes local distortions in the interpolation flow, while the registration loss penalizes the correspondence between the approximation of the target surface ($X(1)$), and the true target surface (ΠY). See section 3.3 of Eisenberger et al. [14] for mathematical formulation of these loss functions. The geodesic loss, which aims to preserve geodesic distances between interpolated surfaces, is not shown; following Eisenberger et al. [14] we set the geodesic loss to 0.0 after epoch 300. Note the y-axis is presented on a logarithmic scale.

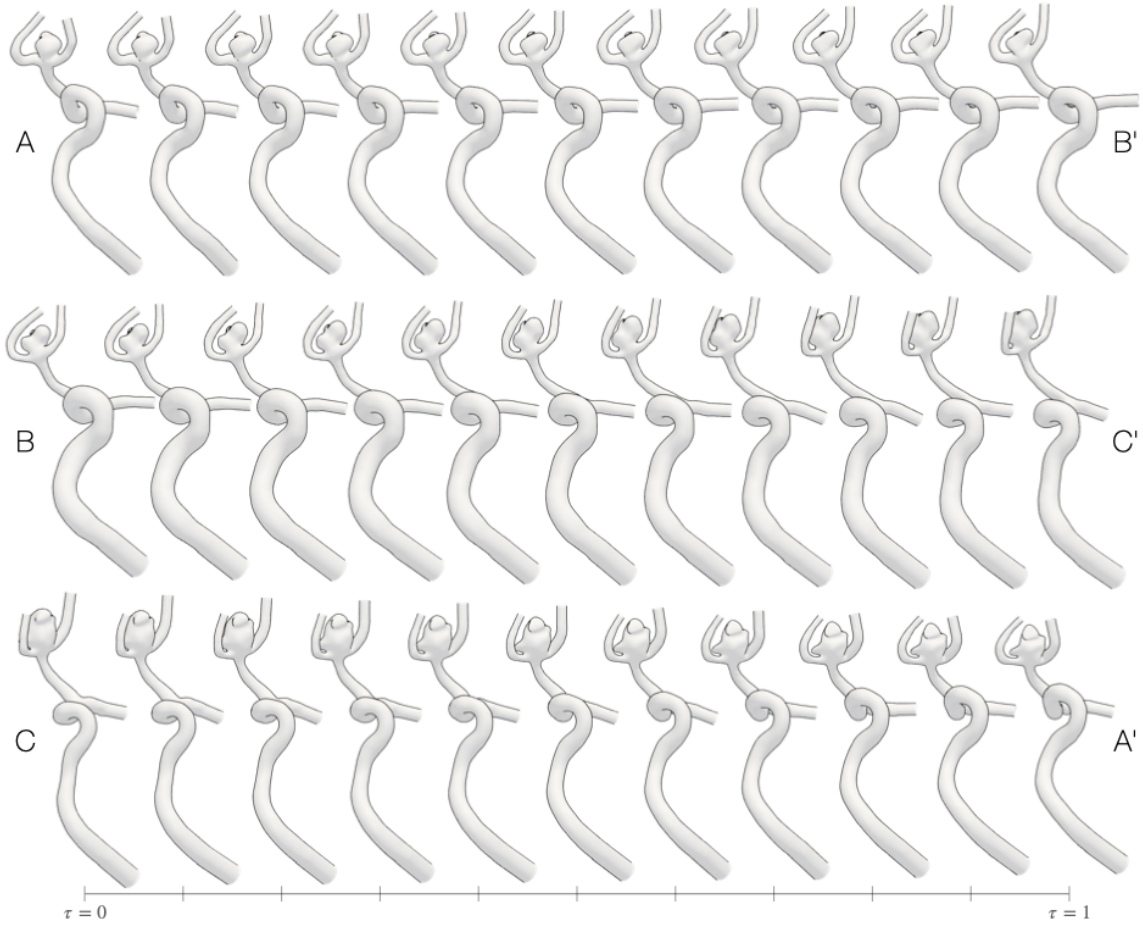

Figure 2: Interpolated surfaces generated from the three original surfaces A, B, and C. These surfaces have been clipped and prepared for CFD.

Table 1: The various morphological and hemodynamic parameters quantified.

Parameter	Description, including units where dimensional, and citation for original formula.
Size	Aneurysm sac size, in mm
A_o	Area of aneurysm ostium, in mm^2
A_{in}	Area of ostium having flow entering (vs exiting), averaged over the cardiac cycle, in mm^2
Q_v	Flow rate in parent vessel, averaged over the cardiac cycle, in mL/s
Q_{in}	Flow rate entering the aneurysm sac, averaged over the cardiac cycle, in mL/s
TAVEL	Time-averaged velocity, spatially averaged over the sac, in m/s
TAWSS	Time-averaged wall shear stress, spatially averaged over the sac, in Pa
LSA	Low shear area, the proportion of the sac exposed to "low" WSS, averaged over the cardiac cycle. Following [27], we define low WSS as being one standard deviation below the mean of WSS the near-vessel region.
ICI	Inflow concentration index, the degree of concentration of the flow stream entering the sac, averaged over the cardiac cycle. Instantaneous $ICI = \frac{Q_{in}/Q_v}{A_{in}/A_o}$
OSI	Oscillatory shear index, spatially averaged over the sac
RRT	Relative residence time, spatially averaged over the sac, in Pa^{-1}
SCI	Shear concentration index, the degree of concentration of "high" WSS on the sac, averaged over the cardiac cycle. Instantaneous $SCI = \frac{F_h/F_a}{A_h/A_a}$ where F is shear force, A is area, and subscripts h and a indicate areas of high shear and the entire sac, respectively [27].
SPI	Spectral power index, the proportion of power from high-frequency temporal fluctuations in velocity magnitude at a given location, relative to the total power of all temporal fluctuations at that location, spatially averaged over the sac [28]
SBI	Spectral bandedness index, a measure of whether velocity fluctuations are broad-banded (SBI $\rightarrow$ 0), suggesting transitional flow, or narrow-banded (SBI $\rightarrow$ 1) suggesting vortex-shedding or other intra-cycle periodicities, spatially averaged over the sac [29]

of Pearson correlation coefficients for each sequence. To identify clusters of consistently correlated parameters, we calculated the average correlation matrix and visualized it using hierarchical clustering (using the `linkage` and texttt-tfcluster methods of `scipy.cluster`).

3 Results

3.1 Qualitative description of hemodynamics for interpolated sequences

As shown in Fig. 3, in all cases the systolic inflow jet enters the sac near the wall in a similar location (left side of each sac), likely reflecting the similarity in curvature of the ACA parent artery segment. All cases demonstrate a region of high TAWSS where the jet impinges on the aneurysm dome, though the size and intensity of these regions vary. Most cases demonstrate turbulent-like flow instabilities, as indicated by high-intensity values in the spectrograms.

In the first interpolation sequence $A \rightarrow B'$, the sac size remains similar throughout while the sac shape and branch angles shift. Over the sequence, the inflow jet intermittently becomes flat and broad ($\tau = 0.4, 1.0$) as opposed to narrow and concentrated ($\tau = 0.0, 0.2$), but generally penetrates the sac to a similar depth throughout. Though the location of the high-TAWSS impingement zone stays generally consistent through the sequence, regions of low TAWSS appear to fade and grow, albeit without changing location. From $\tau = 0.0$ to $\tau = 0.6$, the spectrograms show relatively stable flow with little fluctuation over 100 Hz; after $\tau = 0.6$, high-frequency flow instabilities suddenly emerge, demonstrating moderate harmonic spectral banding indicating intra-cycle flow periodicities.

Through the second interpolation sequence ($B \rightarrow C'$), the sac grows in size and becomes more smooth. The inflow jet is initially confined by the small sac size, wrapping around the aneurysm to connect to the left branch ($\tau = 0.0, 0.2$), then begins to impinge on the sac wall and deflect into the sac center ($\tau = 0.4, 0.6$). After $\tau = 0.6$, the jet remains close to the aneurysm wall, becoming broad and flat. Throughout the sequence, the region of low WSS initially grows (from $\tau = 0.0$ to $\tau = 0.4$), but after $\tau = 0.4$, a region of high-WSS appears within the low-TAWSS region. Despite differences in the aneurysm size and jet structure, the temporal envelope of flow instabilities in the spectrograms remains consistent from $\tau = 0.1$ onward. Moderate harmonic features appear as τ approaches 1, but most cases demonstrate relatively smooth roll-off indicating turbulent-like flow.

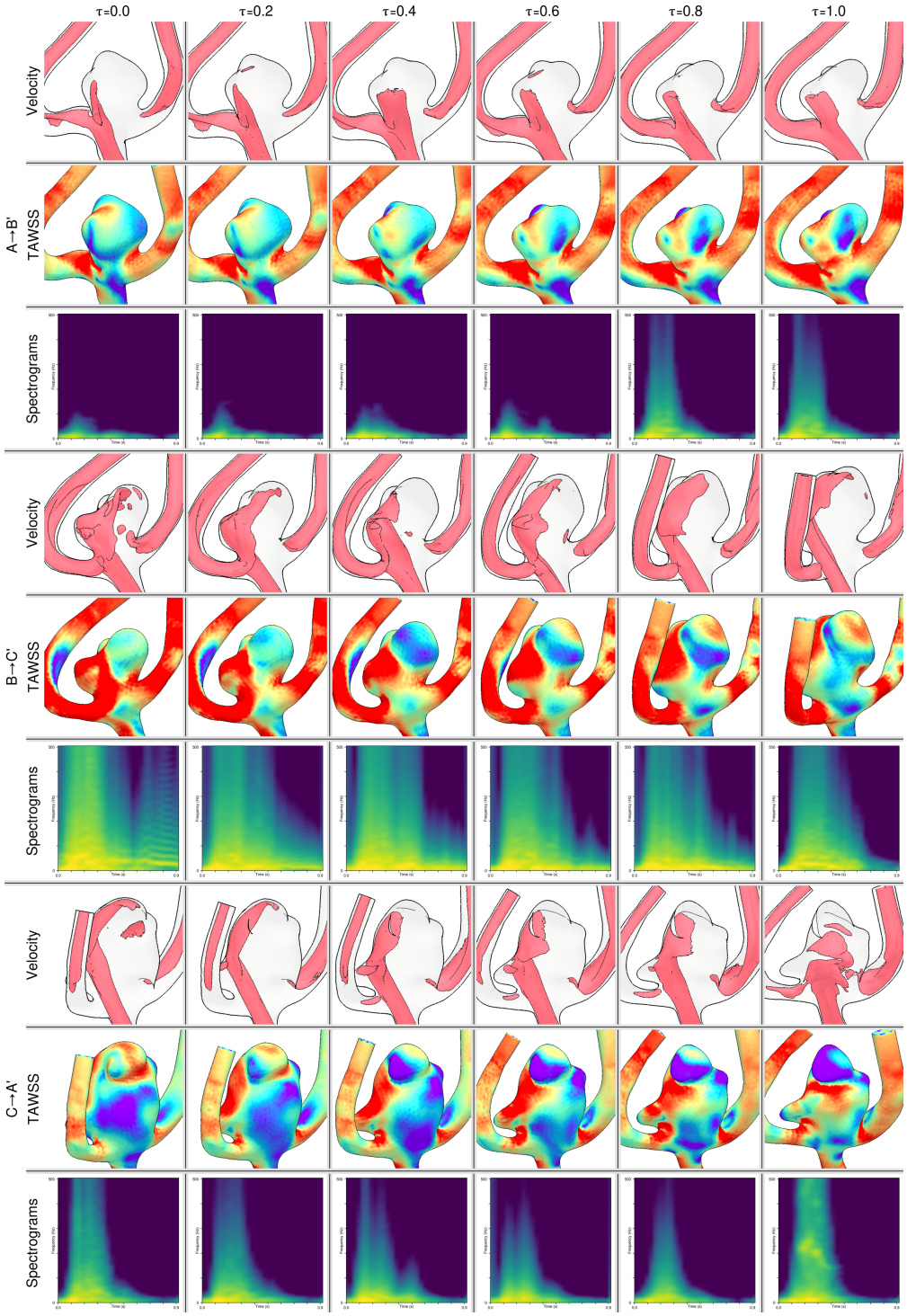

Figure 3: Hemodynamic features of the three interpolated sequences. For each sequence, the top row shows the 0.7 m/s velocity isosurface at peak systole; middle shows the time-averaged wall shear stress (TAWSS), from blue (low) to red (high); and bottom shows the velocity magnitude spectrogram averaged over the sac. Per Eq. (1), τ is the argument of the interpolation flow $\Delta(\tau)$, with data shown above with a spacing of $\tau = 0.2$.

In the interpolation sequence $C \rightarrow A'$, the sac shrinks and becomes more irregular in shape. The inflow jet becomes increasingly more confined, breaking apart as τ approaches 1. The region of low TAWSS on case C initially grows until $\tau = 0.4$, then fades away as another region of low TAWSS appears on the bleb on top of the aneurysm. The intensity of the spectrograms falls from $\tau = 0.0$ to $\tau = 0.6$, then rises until $\tau = 1.0$. At $\tau = 0.4$ and 0.6, the spectral envelope shows two systolic peaks, as opposed to one in the other cases. At $\tau = 1.0$, the spectrogram shows a strong harmonic band decreasing in frequency from 200 Hz to 100 Hz.

3.2 Quantitative hemodynamic trends for interpolated sequences

As shown in Fig. 4, most trends demonstrate relatively smooth change through each interpolation sequence, but these changes are not generally linear or monotonic. In many of the trend lines, hemodynamic parameters evaluated on the interpolated surfaces ($\tau = [0.1, 0.9]$) can fall outside the range of values at the endpoint surfaces ($\tau = 0.0$ and 1.0). As will be discussed later, these trend lines are not contiguous *between* sequences, since the interpolated surface $X(1)$ is only an *approximation* of Y.

As expected, aneurysm sac size (Size) and ostium area (A_o) shift relatively smoothly over each sequence. Inflow area to the sac (A_{in}) is less steady: in sequence 3, A_{in} appears nearly parabolic despite A_o shifting near linearly. Parent artery flow rate (Q_v) shifts smoothly across each sequence, while aneurysm inflow rate (Q_{in}) demonstrates various local extrema within the range $\tau = [0.1, 0.9]$. In each sequence, both Q_v and Q_{in} span a range of only about $\pm 10\%$ of the mean value compared with A_o and A_{in} which span a range of about $\pm 20\%$.

Trends in TAVEL differ in each of the sequences; the first sequence has two peaks, but shows small range; the second decreases nearly monotonically; and the third appears nearly parabolic, reaching a minimum at $\tau = 0.4$, corresponding with the minimum observed in A_{in}. TAWSS is nearly monotonic or constant in all sequences, varying within a range of about $\pm$ 25%. LSA appears slightly more erratic than TAVEL or TAWSS, demonstrating several local extrema, but the variance observed is considerably smaller ($\pm 10\%$ compared with about $\pm 25\%$). ICI for sequence 3 contains a local maximum at $\tau = 0.4$, in agreement with the local minimum observed in TAVEL and A_{in} (as expected given the definition of ICI), otherwise ICI is relatively smooth and appears visually correlated with Q_{in} (again, as expected from its definition).

OSI demonstrates erratic, complex behavior with multiple local extrema across each sequence. RRT, being a combination of TAWSS and OSI, also shows complex behavious with τ, demonstrating a sigmoidal shape in sequence 1, and various local extrema in sequences 2 and 3. Both OSI and RRT vary across a range of about $\pm 50\%$. SCI is only slightly uneven through sequence 1, but varies, within ±100% for sequences 2 and 3, albeit more smoothly than OSI and RRT. SPI is steady across sequence 1 until $\tau = 0.6$, where it increases and plateaus around $\tau = 0.8$; this is also evident in the spectrograms of Fig. 3, which increase in intensity after $\tau = 0.6$. For sequences 2 and 3, SPI is highest at the endpoints, but generally spans a smaller percentile range. SBI is stable across sequence 1, whereas for sequences 2 and 3 there are sharp local changes (250%) near one end, reflecting the harmonic bands observed in Fig. 3.

Fig. 5 visualizes the inter-correlations averaged across the three sequences. As observed already in Fig. 4, Size and A_o are strongly correlated (r=0.88), indicating that NeuroMorph considered both parameters when creating the morphing sequences. Size and A_o also appear correlated with Q_{in} and ICI (r¿0.72). SCI and SBI show moderate negative correlation with Size, A_o, Q_{in}, and ICI, with coefficients ranging from -0.42 to -0.67. For SCI, this could potentially indicate that as aneurysm size increases, the jet momentum does not increase proportionally, resulting in a smaller high-shear concentration zone. For SBI, this could indicate that the jet has stabilized and become less confined, reducing periodic instabilities. Q_v, TAWSS, and TAVEL form a cluster of coefficients ranging from 0.48 to 0.63. SPI is adjacent to this, having r=0.5 with Q_v. This is expected, since, as flow rate in the parent artery increases, sac velocity increases, resulting in higher shear stresses and increased high-frequency instabilities within the sac.

4 Discussion

In this study, we evaluated the sensitivity of CFD-derived hemodynamic parameters to smoothly-shifting and morphologically plausible input geometries that were generated using NeuroMorph. By testing our assumptions about the continuity and sensitivity of hemodynamic parameters in response to changes in geometry, we can learn about the *inter-patient* complexity of these hemodynamic parameters, which may be useful for estimating data requirements or improving the performance of aneurysm rupture prediction models.

By many univariate metrics—size, branch angle, ostium diameter—any two neighboring surfaces within a sequence in Fig. 2 or Fig. 3 vary only slightly, yet in some cases, can generate substantially different hemodynamic responses (as in Figs. 3 and 4). The geometric parameters encapsulated in τ can interact in complex ways to produce potentially divergent flow properties. This would be hard to anticipate in a *sparse* dataset where each morphological descriptor is

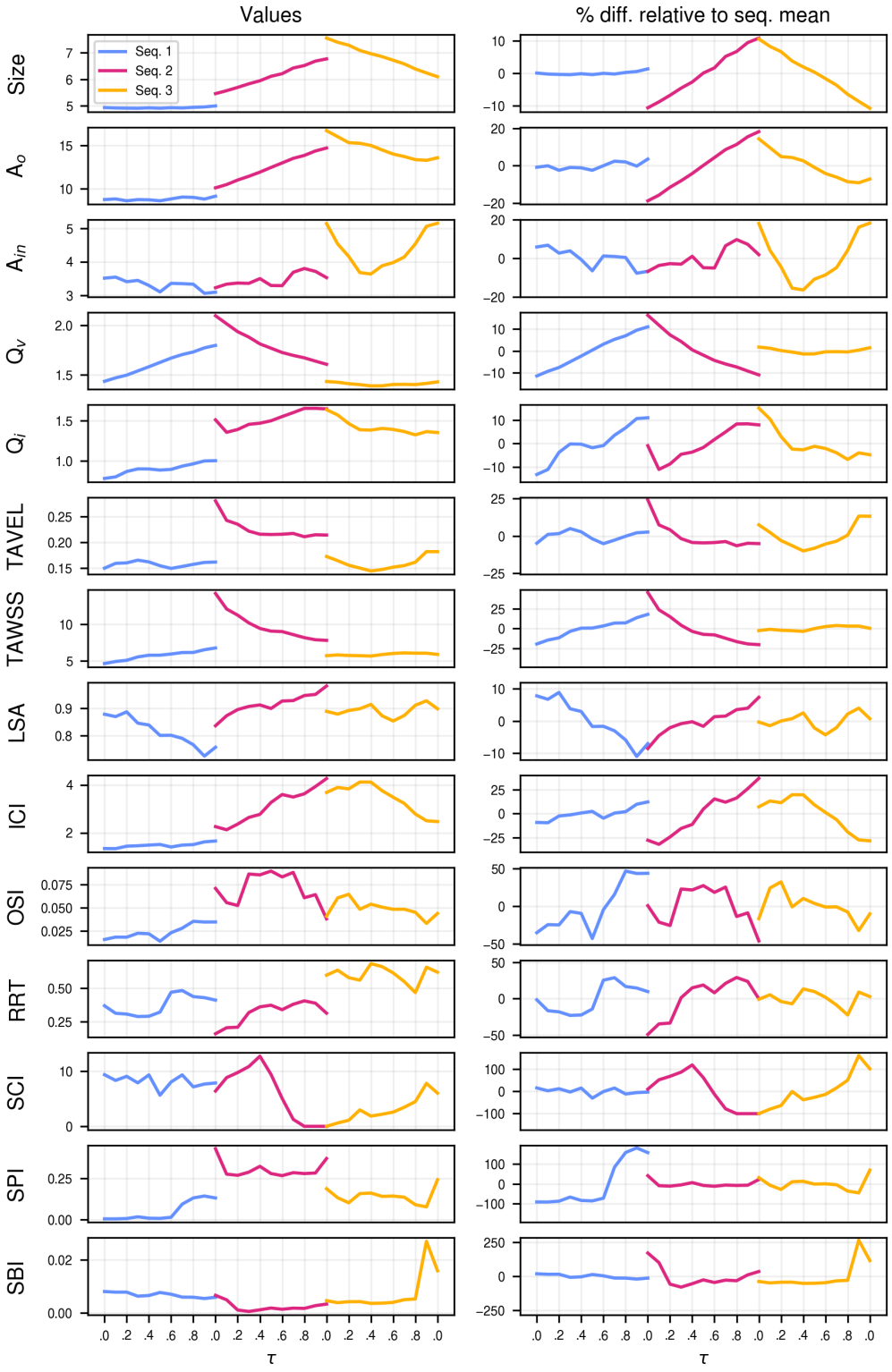

Figure 4: Hemodynamic parameters generated from the interpolated sequences. Percentage-differences were calculated with respect to the sequence mean, as: $100 \times (\text{Mean} - P(\tau))/\text{Mean}$, where $P(\tau)$ are the parameter values across τ, and τ is the argument of the interpolation flow $\Delta(\tau)$.

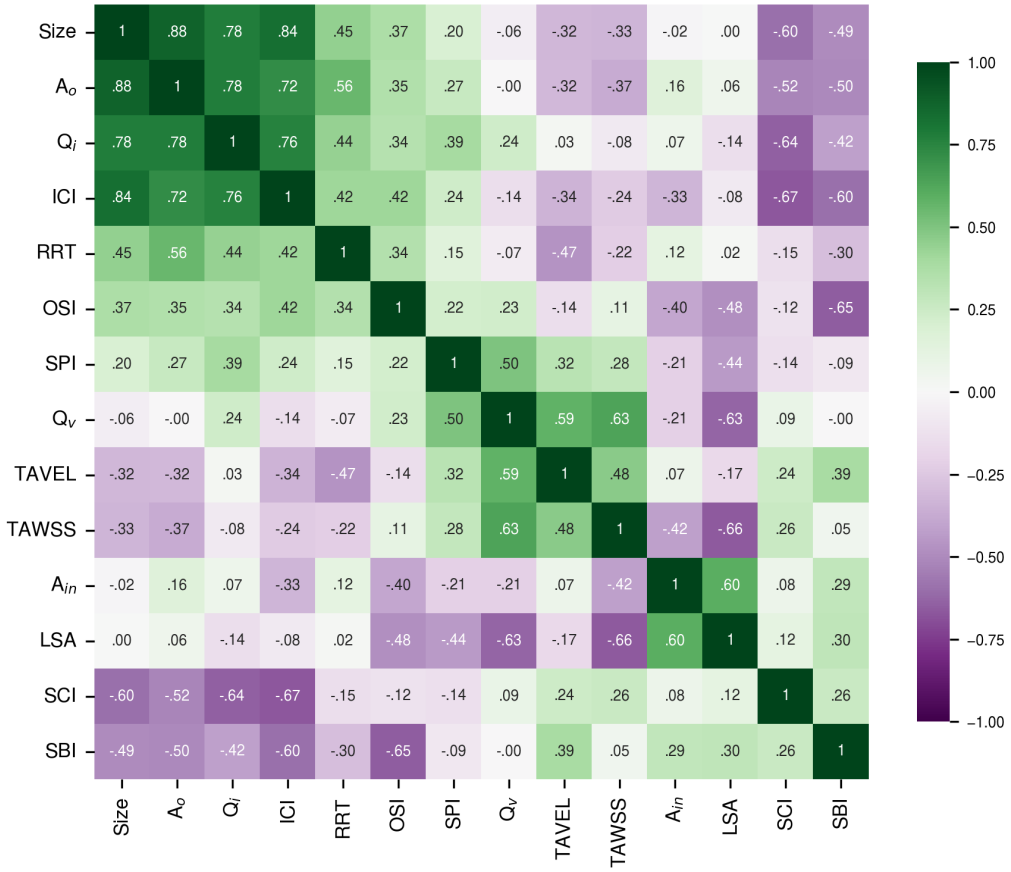

Figure 5: Inter-correlations averaged across the three sequences, and sorted using hierarchical clustering.

tabulated separately, as it would require a multivariate analysis of a large number of geometric parameters (potentially tens or hundreds) and a sufficiently large sample.

4.1 Implications for association and prediction studies

Through each sequence, TAWSS has a "low variation", i.e. nearly monotonic response. As observed in Fig. 4 and Fig. 5, there is a correlation between TAWSS and parent flow rate Q_v; previously, Morales et al. demonstrated that increasing flow rate also increases aneurysm TAWSS [30], and our results confirm this relationship in the presence of complex morphological interactions. Since Q_v can be robustly estimated from geometry-based 0D circuit models [31], this may suggest that TAWSS could be estimated similarly. By contrast, OSI has a relatively "high variation" response, demonstrating steep slopes and local extrema over the interpolated range. Consider sequence 2: OSI increases about 50% between $\tau = 0.2$ and $\tau = 0.3$, and the value at $\tau = 0.3$ is about 25% greater than the value at endpoints $\tau = 0.0$ or $\tau = 1.0$. This would be difficult to anticipate in a real-world sparse dataset, which may indicate that OSI has high modelling uncertainty and is not a robustly measurable candidate for rupture prediction or association studies, or would at least require a large dataset to fully characterize. These results echo previous studies that have demonstrated high sensitivity in OSI to flow rate [32], imaging modality [33], waveform and outflow conditions [34], and segmentation of the aneurysm neck [17]. This limited robustness in OSI may help explain discrepancies between rupture association studies: in a review of hemodynamic parameters in 46 studies [35], Liang et al. identified that OSI was positively associated with rupture in only 5/16 studies in which it appeared. LSA and TAWSS (which

ranked 1st and 2nd in [35]) may perform comparatively better due to their relative robustness—LSA only varies by about 10% across any sequence in the current study and is relatively smooth; TAWSS exhibits greater range, but is smoother still. Association studies based on these parameters may be more consistent between studies because the *inter-patient* complexity of these parameters is lower than parameters such as OSI. This stability, however, could potentially "cut both ways"—recent literature suggests that conventional hemodynamic parameters may add little value relative to easier-to-measure morphological parameters for use in rupture prediction or association studies [36, 37, 4, 8]. We suspect that some hemodynamic parameters, such as TAWSS and LSA may contain a high degree of *mutual information* with common morphological parameters; this implies that, in order for hemodynamic parameters to substantially outperform morphological parameters for rupture prediction, they must contain *additional* information.

SCI shifts relatively smoothly over each sequence, but demonstrates a prominent local maximum at $\tau = 0.4$ in sequence 2—this could indicate that SCI provides additional information over the parameters that shift monotonically over τ, such as Size, Q_v, or TAWSS. As such, this could also indicate that large datasets are needed to reveal associations with rupture, and may explain discrepancies where rupture association with the parameters was found in large datasets (N = 210[38], N = 784 [5], N = 1931 [39]), but not in small datasets (N = 50, as in [29]).

4.2 Insights into flow (in)stability

These hemodynamic parameters reveal insight into the development of flow instabilities: in sequence 1, SPI sharply increases between $\tau = 0.6$ and $\tau = 0.8$ suggesting the spontaneous development of turbulent-like instabilities in response to changes in geometry (and geometry-derived inflow rate, which resulted in a modest increase in Q_v of $\sim 5\%$). Previously, Khan et al. demonstrated a similar "tipping point", whereby SPI_{WSS} sharply increased by nearly 500% in response to a 25% increase in flow rate [28]. Compared with TAWSS, which shifted nearly linearly across each sequence, this change is sudden, but not as erratic as changes observed in OSI. The parameters that we consider measures of flow complexity (SPI, OSI, SCI) do not necessarily correlate: for example, SPI increases after $\tau = 0.6$ in response to destabilization of the inflow jet, but since the jet concentration on the wall did not meaningfully change (as is evident in the size and penetration of the jet in Fig. 3), SCI remained constant. In sequence 2, the reverse is observed: SPI shows relatively little variation, but SCI demonstrates a local maxima at $\tau = 0.4$ (100% greater than SCI values at the endpoints $\tau = 0.0$ or 1.0) followed by a steep decrease. In this case, SCI[2] appears to be affected by (1) the size of the aneurysm and (2) by the jet proximity to the wall; from $\tau = 0.0$ to $\tau = 0.4$, the sac area grows (while impingement zone stays near constant), which contributes to an *increase* in SCI; after $\tau = 0.4$, the jet transitions to be closer to the wall, increasing the ratio of A_h/A_a and thereby *decreasing* SCI. OSI and SCI demonstrate correlation in sequence 1, but weak correlation in sequence 2 and 3. Among these three parameters, the greatest average Pearson correlation was only 0.22.

4.3 Inter-correlations and identifying redundancies

In Liang et al. [35], the authors identified 81 morphological and hemodynamic parameters used across 46 studies; this broad variety in reported measures has also been critically described as "alphabet soup" [40], with those authors advocating for more studies to focus on parameters of hypothesis-driven mechanisms. Hierarchical cluster analysis of correlations, as in Fig. 5, has been previously used to identify relationships and redundancies between hemodynamic and morphological parameters before and after stent placement [41]. This analysis may also be useful for sorting the "alphabet soup" of parameters used for rupture prediction. For example, in a study of N = 1931 aneurysms [3], Detmer et al. indicated that *nearly all* of the 49 hemodynamic parameters tested were associated with rupture, including Size, ICI, Q_{in}, and A_{ostium}: in the present study, we see that these parameters are highly correlated (Fig. 4), as expected given the definition of ICI. Future studies should consider using hierarchical clustering of correlation coefficients to reduce redundancy in reported parameters.

4.4 Plausibility of interpolated morphologies

In each of the interpolated sequences, morphological features gradually shift over τ, but the surfaces at $\tau = 1.0$ are only an approximation of the true target surface. As such, there are non-negligible differences between the patient-derived surfaces (A, B, C) and the approximated surfaces (A', B', C') in Fig. 2 that disrupt direct comparison of hemodynamics. For example, though B and B' share strong visual similarities in Fig. 2, B has both a larger inlet diameter (4.9 mm vs 4.3 mm) and a narrower ACA segment (1.7 mm vs 2.1 mm), which contributes to the development of highly unstable flow with prominent harmonic instabilities during diastole that are not present in B' (Fig. 3). These differences between the target surface and the approximated surface are a byproduct of NeuroMorph, as observed in

[2] $SCI = \frac{F_h/F_a}{A_h/A_a}$, where F is total shear force, A is area, and subscripts h and a represent the domain of high shear and the entire aneurysm, respectively.

Eisenberger et al.'s first figure [14]. These differences further highlight the sensitivity of hemodynamics to geometry—B and B' look very similar, but have considerably different hemodynamic properties.

Real-world aneurysms demonstrate large variation in size and shape [42]. In the present work, most of the aneurysms appear *plausible*, but as τ increases, the sac shapes do not necessarily reflect the mechanobiological processes that drive real aneurysm growth. For example, in sequence 3 at $\tau = 1.0$, the jet impinges on a concavity of the aneurysm sac, driving complex, harmonic instabilities. Given that jet impingement (via SCI) has been shown to be associated with aneurysm growth [5], we might not expect the impingement zone to be concave, which may expose the fact that the surface was synthetically generated. Despite this, in sequence 3, common parameters such as TAWSS and LSA hardly change in Fig. 4—in Figs. 4 and 5, we also see that both LSA and TAWSS are more correlated with Q_v than with Size or A_o, suggesting a potential insensitivity of LSA and TAWSS to morphological descriptions of the sac. As such, even if the sacs were *unrealistic*, the current sensitivity analysis still provides insight into the behavior of hemodynamic parameters in response to changes in geometry.

In this paper, we evaluated sequences between three pairs of patient-derived surfaces. As such, the trends in Fig. 4 and correlations in Fig. 5 may not necessarily generalize to other sequences. We chose three surfaces in order to: (1) evaluate NeuroMorph's learning capability on small datasets; (2) explore whether overfitting NeuroMorph produced improved correspondence matrices, and; (3) to limit the complexity that is possible with large datasets. To address (1), NeuroMorph produced generally plausible surfaces given the limited data, but (2) overfitting did not appear to drive the solution towards a "perfect" morph (as is evident by the limited approximation of Y by $X(1)$ in each sequence). If this experiment was extended to more training surfaces (as (3) implies), we could generate $\binom{n}{2}$ pairs, where n is the number of surfaces; 10 surfaces would generate 45 pairs, while 100 would generate nearly 5000, and each pair could be used to generate a sequence as in Fig. 2. Our overfitting strategy (75 000 epochs) took ∼4 days to train, but as shown in Fig. 1, the network achieved near equivalent results after $\sim$ 20 000 epochs, or about 1 day of training. To reduce training time when using more surfaces, it may be useful to extend our non-uniform remeshing strategy by further reducing the number of vertices in regions of relatively low curvature, such as the ICA segment. In the original paper, Eisenburger et al. demonstrate how NeuroMorph-generated interpolations can be used to *augment* small datasets to a size large enough to train more-general implicit networks such as [43], which could in-turn be used for various shape-analysis tasks. In the context of cerebrovascular surface datasets, a general latent representation of the morphology could be useful as a basis for hemodynamic surrogate modelling or identifying similar surfaces.

4.5 Potential limitations

Our study was limited to training on 3 cases, specifically chosen to highlight potential sensitivities of hemodynamic parameters to geometry. As such, these sensitivities are what *could* be the case, not necessarily what *would* be the case, for any particular cohort of aneurysms. Nevertheless, our proof-of-principle computer experiment highlights how a neural network like NeuroMorph, eventually trained on a larger number of datasets, could be used to draw broader conclusions about the relationship between morphology and hemodynamics.

Using our chosen inflow strategy $Q_{avg} \propto D^2$ (as described in [44]), each case-specific flow rate is determined by the inlet ICA diameter, which changes across each sequence. Flow rate has been demonstrated to have a considerable effect on hemodynamic parameters [32], and the trends we observed may differ at different flow rates, or using different inflow recipes. However, this recipe reflects the fact that patient-specific flow rates are often unavailable for CFD modelling, and the chosen strategy has been demonstrated to minimize errors relative to patient-specific flow rates. Future studies should incorporate the variability of flow rate when looking at sensitivity as in Fig. 4 or inter-correlations as in Fig. 5.

Deep neural networks, such as NeuroMorph, have many tunable hyperparameters. In [14], Eisenberger et al. tuned NeuroMorph's hyperparameters on a validation set, and subsequently used the same hyperparameters for all experiments. To be consistent with this work, we used the default hyperparameters chosen by Eisenberger, which includes setting the geodesic loss l_{geo} to 0 after a threshold number of iterations. Eisenberger et al. note that this loss component is used to guide the network early in the training process, but can hinder training for extremely non-isometric pairs. We suspect that tuning this parameter (or others) may improve the generation of the correspondence matrix, which could reduce the differences observed between the target surfaces (A, B, C) and approximated surfaces (A', B', C').

5 Conclusion

We applied an unsupervised deep-learning method for 3D shape interpolation (NeuroMorph) to intracranial aneurysm datasets and demonstrated the sensitivity and continuity of various hemodynamic parameters to non-specific changes in morphology. We demonstrated that some parameters such as LSA and TAWSS are only modestly affected by large

changes in morphology, while other parameters such as OSI show high variation between seemingly similar surfaces. This balance of robustness vs. sensitivity has implications for clinical applications of these parameters: parameters that are highly "robust" may be non-specific to the aneurysm environment, while parameters that are highly sensitive to geometry may also be highly uncertain, limiting clinical application. Understanding these sensitivities could help identify parameters that provide utility over easier-to-measure morphological parameters.

6 Acknowledgements

This work was supported by a grant to DAS from the Natural Sciences & Engineering Research Council of Canada (RGPIN-2018-04649). DEM acknowledges the generous support of an Ontario Graduate Scholarship and a Barbara & Frank Milligan Graduate Fellowship. VMP acknowledges the generous support from Michael's Family; a JDMI/UHN Research Leadership Award; and the Schroeder Chair in Advanced Neurovascular Interventions. Computations were performed on the Niagara supercomputer at the SciNet HPC Consortium. SciNet is funded by: the Canada Foundation for Innovation; the Government of Ontario; Ontario Research Fund—Research Excellence; and the University of Toronto.

7 Nomenclature

References

[1] H. Meng et al. "High WSS or Low WSS? Complex Interactions of Hemodynamics with Intracranial Aneurysm Initiation, Growth, and Rupture: Toward a Unifying Hypothesis". In: *American Journal of Neuroradiology* 35.7 (July 2014), pp. 1254–1262. DOI: 10.3174/ajnr.A3558.

[2] V. L. Rayz and A. A. Cohen-Gadol. "Hemodynamics of cerebral aneurysms: connecting medical imaging and biomechanical analysis". In: *Annual review of biomedical engineering* 22 (2020), pp. 231–256.

[3] F. J. Detmer et al. "Comparison of statistical learning approaches for cerebral aneurysm rupture assessment". In: *International Journal of Computer Assisted Radiology and Surgery* 15.1 (Jan. 2020), pp. 141–150. DOI: 10.1007/s11548-019-02065-2.

[4] S. Tanioka et al. "Machine Learning Classification of Cerebral Aneurysm Rupture Status with Morphologic Variables and Hemodynamic Parameters". In: *Radiology: Artificial Intelligence* 2.1 (Jan. 2020), e190077. DOI: 10.1148/ryai.2019190077.

[5] B. Chung et al. "Identification of Hostile Hemodynamics and Geometries of Cerebral Aneurysms: A Case-Control Study". In: *American Journal of Neuroradiology* 39.10 (Oct. 2018), pp. 1860–1866. DOI: 10.3174/ajnr.A5764.

[6] D. A. Steinman and V. M. Pereira. "How patient specific are patient-specific computational models of cerebral aneurysms? An overview of sources of error and variability". In: *Neurosurgical Focus* 47.1 (July 2019), E14. DOI: 10.3171/2019.4.FOCUS19123.

[7] P. Berg et al. "A review on the reliability of hemodynamic modeling in intracranial aneurysms: why computational fluid dynamics alone cannot solve the equation". In: *Neurosurgical Focus* 47.1 (July 2019), E15. DOI: 10.3171/2019.4.FOCUS19181.

[8] N. Juchler et al. "Shape Trumps Size: Image-Based Morphological Analysis Reveals That the 3D Shape Discriminates Intracranial Aneurysm Disease Status Better Than Aneurysm Size". In: *Frontiers in Neurology* 13 (May 2022), p. 809391. DOI: 10.3389/fneur.2022.809391.

[9] A. Lauric et al. "Proximal Parent Vessel Tapering is Associated With Aneurysm at the Middle Cerebral Artery Bifurcation". In: *Neurosurgery* 84.5 (May 2019), pp. 1082–1089. DOI: 10.1093/neuros/nyy152.

[10] A. Lauric et al. "Aneurysm presence at the anterior communicating artery bifurcation is associated with caliber tapering of the A1 segment". In: *Journal of Neurosurgery* 136.6 (June 2022), pp. 1694–1704. DOI: 10.3171/2021.5.JNS204389.

[11] J. Brüning et al. "Uncertainty Quantification for Non-invasive Assessment of Pressure Drop Across a Coarctation of the Aorta Using CFD". In: *Cardiovascular Engineering and Technology* 9.4 (Dec. 2018), pp. 582–596. DOI: 10.1007/s13239-018-00381-3.

[12] H. Kjeldsberg, A. Bergersen, and K. Valen-Sendstad. "morphMan: Automated manipulation of vascular geometries". In: *Journal of Open Source Software* 4.35 (Mar. 2019), p. 1065. DOI: 10.21105/joss.01065.

[13] K. Capellini et al. "Computational Fluid Dynamic Study for aTAA Hemodynamics: An Integrated Image-Based and Radial Basis Functions Mesh Morphing Approach". In: *Journal of Biomechanical Engineering* 140.11 (Nov. 2018), p. 111007. DOI: 10.1115/1.4040940.

[14] M. Eisenberger et al. "NeuroMorph: Unsupervised Shape Interpolation and Correspondence in One Go". In: *2021 IEEE/CVF Conference on Computer Vision and Pattern Recognition (CVPR)*. Nashville, TN, USA: IEEE, June 2021, pp. 7469–7479. DOI: 10.1109/CVPR46437.2021.00739. URL: https://ieeexplore.ieee.org/document/9578426/ (visited on 06/21/2022).

[15] B. Deng et al. "A Survey of Non-Rigid 3D Registration". In: *Computer Graphics Forum* 41.2 (May 2022), pp. 559–589. DOI: 10.1111/cgf.14502.

[16] D. E. MacDonald et al. "Improving visualization of three-dimensional aneurysm features via segmentation with upsampled resolution and gradient enhancement (SURGE)". In: *Journal of NeuroInterventional Surgery* (June 2022), neurintsurg–2022–018912. DOI: 10.1136/neurintsurg-2022-018912.

[17] D. E. MacDonald et al. "Aneurysm Neck Overestimation has a Relatively Modest Impact on Simulated Hemodynamics". In: *Cardiovascular Engineering and Technology* 14.2 (2023), pp. 252–263.

[18] A. Vedaldi. *NeuroMorph: Unsupervised Shape Interpolation and Correspondence in One Go*. July 2022. URL: https://github.com/facebookresearch/neuromorph (visited on 07/27/2022).

[19] C. Sullivan and A. Kaszynski. "PyVista: 3D plotting and mesh analysis through a streamlined interface for the Visualization Toolkit (VTK)". In: *Journal of Open Source Software* 4.37 (May 2019), p. 1450. DOI: 10.21105/joss.01450.

[20] C. R. Harris et al. "Array programming with NumPy". In: *Nature* 585.7825 (Sept. 2020), pp. 357–362. DOI: 10.1038/s41586-020-2649-2.

[21] P. Virtanen et al. "SciPy 1.0: fundamental algorithms for scientific computing in Python". In: *Nature Methods* 17.3 (Mar. 2020), pp. 261–272. DOI: 10.1038/s41592-019-0686-2.

[22] M. Hogg. *pygeodesic: Python library to compute geodesic distance over a triangular based surface mesh*. July 2022. URL: https://github.com/mhogg/pygeodesic (visited on 08/08/2022).

[23] S. Valette, J.-M. Chassery, and R. Prost. "Generic Remeshing of 3D Triangular Meshes with Metric-Dependent Discrete Voronoi Diagrams". In: *IEEE Transactions on Visualization and Computer Graphics* 14.2 (Mar. 2008), pp. 369–381. DOI: 10.1109/TVCG.2007.70430.

[24] M. Attene. "A lightweight approach to repairing digitized polygon meshes". In: *The Visual Computer* 26.11 (Nov. 2010), pp. 1393–1406. DOI: 10.1007/s00371-010-0416-3.

[25] R. Izzo et al. "The Vascular Modeling Toolkit: A Python Library for the Analysis of Tubular Structures in Medical Images". In: *Journal of Open Source Software* 3.25 (May 2018), p. 745. DOI: 10.21105/joss.00745.

[26] M. O. Khan, K. Valen-Sendstad, and D. A. Steinman. "Narrowing the Expertise Gap for Predicting Intracranial Aneurysm Hemodynamics: Impact of Solver Numerics versus Mesh and Time-Step Resolution". In: *American Journal of Neuroradiology* 36.7 (July 2015), pp. 1310–1316. DOI: 10.3174/ajnr.A4263.

[27] F. Mut et al. "Computational hemodynamics framework for the analysis of cerebral aneurysms". In: *International Journal for Numerical Methods in Biomedical Engineering* 27.6 (June 2011), pp. 822–839. DOI: 10.1002/cnm.1424.

[28] M. O. Khan et al. "On the quantification and visualization of transient periodic instabilities in pulsatile flows". In: *Journal of Biomechanics* 52 (Feb. 2017), pp. 179–182. DOI: 10.1016/j.jbiomech.2016.12.037.

[29] D. E. MacDonald et al. "Spectral Bandedness in High-Fidelity Computational Fluid Dynamics Predicts Rupture Status in Intracranial Aneurysms". In: *Journal of Biomechanical Engineering* 144.6 (June 2022), p. 061004. DOI: 10.1115/1.4053403.

[30] H. G. Morales and O. Bonnefous. "Unraveling the relationship between arterial flow and intra-aneurysmal hemodynamics". In: *Journal of Biomechanics* 48.4 (Feb. 2015), pp. 585–591. DOI: 10.1016/j.jbiomech.2015.01.016.

[31] C. Chnafa et al. "Better Than Nothing: A Rational Approach for Minimizing the Impact of Outflow Strategy on Cerebrovascular Simulations". In: *American Journal of Neuroradiology* 39.2 (Feb. 2018), pp. 337–343. DOI: 10.3174/ajnr.A5484.

[32] M. Najafi et al. "How patient-specific do internal carotid artery inflow rates need to be for computational fluid dynamics of cerebral aneurysms?" In: *Journal of NeuroInterventional Surgery* 13.5 (May 2021), pp. 459–464. DOI: 10.1136/neurintsurg-2020-015993.

[33] N. M. Cancelliere et al. "4D-CT angiography versus 3D-rotational angiography as the imaging modality for computational fluid dynamics of cerebral aneurysms". In: *Journal of NeuroInterventional Surgery* 12.6 (June 2020), pp. 626–630. DOI: 10.1136/neurintsurg-2019-015389.

[34] H. Rajabzadeh-Oghaz et al. "Inter-patient variations in flow boundary conditions at middle cerebral artery from 7T PC-MRI and influence on Computational Fluid Dynamics of intracranial aneurysms". In: *Computers in Biology and Medicine* 120 (May 2020), p. 103759. DOI: 10.1016/j.compbiomed.2020.103759.

[35] L. Liang et al. "Towards the Clinical utility of CFD for assessment of intracranial aneurysm rupture – a systematic review and novel parameter-ranking tool". In: *Journal of NeuroInterventional Surgery* 11.2 (Feb. 2019), pp. 153–158. DOI: 10.1136/neurintsurg-2018-014246.

[36] J. Xiang et al. "Hemodynamic–morphological discriminant models for intracranial aneurysm rupture remain stable with increasing sample size". In: *Journal of NeuroInterventional Surgery* 8.1 (2014), pp. 104–110. DOI: 10.1136/neurintsurg-2014-011477.

[37] J. Schneiders et al. "Additional Value of Intra-Aneurysmal Hemodynamics in Discriminating Ruptured versus Unruptured Intracranial Aneurysms". In: *American Journal of Neuroradiology* 36.10 (Oct. 2015), pp. 1920–1926. DOI: 10.3174/ajnr.A4397.

[38] J. Cebral et al. "Quantitative Characterization of the Hemodynamic Environment in Ruptured and Unruptured Brain Aneurysms". In: *American Journal of Neuroradiology* 32.1 (Jan. 2011), pp. 145–151. DOI: 10.3174/ajnr.A2419.

[39] F. J. Detmer et al. "Associations of hemodynamics, morphology, and patient characteristics with aneurysm rupture stratified by aneurysm location". In: *Neuroradiology* 61.3 (Mar. 2019), pp. 275–284. DOI: 10.1007/s00234-018-2135-9.

[40] M. R. Levitt et al. "One way to get there". In: *Journal of NeuroInterventional Surgery* 13.5 (May 2021), pp. 401–402. DOI: 10.1136/neurintsurg-2021-017559.

[41] C. Karmonik et al. "Relationships and redundancies of selected hemodynamic and structural parameters for characterizing virtual treatment of cerebral aneurysms with flow diverter devices". In: *Journal of Biomechanics* 49.11 (July 2016), pp. 2112–2117. DOI: 10.1016/j.jbiomech.2015.11.035.

[42] M. L. Raghavan, B. Ma, and R. E. Harbaugh. "Quantified aneurysm shape and rupture risk". In: *Journal of Neurosurgery* 102.2 (Feb. 2005), pp. 355–362. DOI: 10.3171/jns.2005.102.2.0355.

[43] A. Gropp et al. *Implicit Geometric Regularization for Learning Shapes*. July 2020. URL: http://arxiv.org/abs/2002.10099 (visited on 07/13/2022).

[44] C. Chnafa et al. "Errors in power-law estimations of inflow rates for intracranial aneurysm CFD". In: *Journal of Biomechanics* 80 (Oct. 2018), pp. 159–165. DOI: 10.1016/j.jbiomech.2018.09.006.